Opto-Electronic Advances

CN 51-1781/TN ISSN (Print) 2096-4579 ISSN (Online) 2097-3993

Active retinal projection augmented reality display via pixel-to-pixel collimation

Xiang Zhang, Yuanlong Huang, Weiyao Fan, Enguo Chen and Jiajun Luo*

Citation: Zhang X, Huang YL, Fan WY, Fan EG, Luo JJ. Active retinal projection augmented reality display via pixel-to-pixel collimation. *Opto-Electron Adv* **9**, 250252 (2026).

https://doi.org/10.29026/oea.2026.250252

Received: 21 September 2025; Accepted: 9 January 2026; Published online: 28 February 2026

OEA | Opto-Electronic Advances

Article

May 2026, Vol. 9, No. 5

Open Access

Active retinal projection augmented reality display via pixel-to-pixel collimation

Xiang Zhang[1†], Yuanlong Huang[1†], Weiyao Fan[1], Enguo Chen[2] and Jiajun Luo[1*]

Abstract: As the next-generation human–computer interface, augmented reality display technology has been gradually popular, depending on advances in system architectures. However, existing waveguide and passive retinal projection display solutions are unable to combine their respective advantages to address increasingly demanding performance requirements. Herein, we propose an active retinal projection display (A-RPD) concept based on collimated active-matrix microdisplay panels. By deriving and validating the collimation-dependent depth of focus, the optimization direction of this architecture is emphasized. Through the direct integration of pixel-to-pixel collimators on the microdisplay panels, an A-RPD prototype featuring a balanced design and performance has been successfully constructed. It enables clear retinal imaging from 40 cm to 160 cm, which significantly surpasses that of the uncollimated microdisplay. The proposed active retinal projection architecture retains the advantages of retinal projection while simplifying the architecture. This work highlights its importance and superiority and provides foundations for its further expansion in practical applications.

Keywords: retinal projection display; augmented reality display; optical design; display

DOI: 10.29026/oea.2026.250252 | CSTR: 32247.14.oea.2026.250252

Citation: Zhang X, Huang YL, Fan WY et al. Active retinal projection augmented reality display via pixel-to-pixel collimation. *Opto-Electron Adv* **9**, 250252 (2026).

1 Introduction

Visual perception is a critical pathway for humans to expand their cognition of the surroundings, driving the continuous advancement of display technologies from flat-panel displays to near-eye displays[1–3]. Augmented reality (AR) display stands out as one of the most typical representatives in this evolution, serving as an interface to bridge the virtual and the real worlds[4,5]. In the pursuit of next-generation AR displays, the human-centered philosophy encourages continuous efforts toward immersive, comfortable, and portable morphology[6–9]. In recent years, substantial progress has been achieved in lightweight devices and the significantly mitigated "screen-door effect"[10–13]. However, the current solutions are mainly occupied by the virtual image projection, making the vergence-accommodation conflict (VAC) an unavoidable issue[1,14,15].

Based on the principle of the Maxwellian view, projecting images directly onto the retina through a light beam passing through the pupil center could be a promising solution to relieve the VAC[16,17]. The AR devices based on this principle are called retinal projection display (RPD)[18,19]. Traditional RPDs typically involve easily collimated point light sources and spatial light modulators (SLMs), such as liquid crystals on silicon (LCoS)[20,21]. Alternatively, highly collimated lasers were employed for image projection through rapid scanning and deflection enabled by micro-electro-mechanical systems (MEMS)[22,23]. These RPDs requiring a collimated light source to pass through image sources, similar to the principle of liquid crystal displays (LCDs), are defined as passive RPDs (P-RPDs). P-RPD represents a compromise for the traditional active-matrix (AM) surface light sources due to their difficulties in light collimation.

As the size of light-emitting diodes (LEDs) continues to downscale, display panels are usually regarded as

Received: 21 September 2025

Accepted: 9 January 2026

Published online: 28 February 2026

[1]Wuhan National Laboratory for Optoelectronics (WNLO) and School of Optical and Electronic Information, Huazhong University of Science and Technology (HUST), 1037 Luoyu Road, Wuhan 430074, China; [2]National & Local United Engineering Laboratory of Flat Panel Display Technology and College of Physics and Information Engineering, Fuzhou University (FZU), Fuzhou 350108, China.

†These authors contributed equally to this work.

*Correspondence: JJ Luo, E-mail: luojiajun@hust.edu.cn

well-arranged point light source arrays[24–27]. The microscale display panels with downscaled LEDs offer opportunities for the integration of emerging micro-nano structures, enabling direct output of images with collimated light beams[28–30]. Utilizing integrated light sources for direct image projection on the retina instead of additional image sources is proposed here as active RPD (A-RPD). Unlike P-RPDs, A-RPDs hold the potential to achieve smaller volumes, greater comfort, and laser-free damage. However, the A-RPD reinvigorated by microdisplay panels is still in its preliminary stage with unclear architecture and inadequate understanding of collimation-influenced depth of focus (DOF). Lacking standardization and theoretical frameworks for the A-RPD architecture will severely hinder its future development.

Here, we propose the concept of A-RPD with whose performance is highly impacted by the collimation of integrated light sources. This concept with simplified architecture is enabled by emerging AM microdisplay panels for their potential in the integration of image sources and collimated light sources. Based on this, we further derive the relationship between DOF and the exit pupil size influenced by the collimation of microdisplay panels. We then validated the derivation by simulating and demonstrating the A-RPD prototype with a balanced design and performance based on AM microdisplay panels collimated at the pixel level. The constructed A-RPD prototype enables clear retinal imaging wherever the human eye focuses on objects within the range from 40 cm to 160 cm. This work highlights the importance and superiority of A-RPDs achieved by collimated AM microdisplay panels and provides foundations for their further expansion in practical applications.

2 Main

2.1 Concept of passive and active RPDs

Passive displays, typically featuring the architecture with a separated image source and light source, have matured as commercial solutions in various display applications due to their ability to alleviate the burden on the light source[31]. However, the introduced image sources typically come at the expense of some crucial performance, including system efficiency, overall volume, response speed, and contrast ratio[32–34]. Passive displays are gradually losing ground in emerging display applications since the trade-offs between performance and form-factor requirements become increasingly severe. Currently, the emerging active displays present the potential to replace the traditional choices for higher performance and small volume. The achievement of light-emitting diodes (LEDs) with active-matrix drivers has enabled the better integration of image sources and light sources, thereby accelerating related advances[35–37]. This trend is especially obvious in flat-panel displays and projection displays during their evolution towards miniaturization. Similarly, active display solutions will probably bring significant advantages to next-generation AR displays, yet still lack comprehensive discussions and emphasis in RPDs.

In AR displays, the RPD architecture is commonly employed to mitigate the VAC problem[38]. The traditional architecture involves separated image sources, such as LCoS and digital micromirror device (DMD)[22,39]. This configuration arises from the realization of RPDs requiring collimated light beams to pass through the pupil center, and the additional image source allows the employment of collimated point light sources. This RPD architecture, analogous to traditional LCDs, is herein defined as P-RPD (Fig. 1(a)).

Unlike P-RPD, A-RPD, firstly defined here, involves direct integration of pixelated light sources and collimators to provide patterned and collimated light emission (Fig. 1(b)). The downscaled LEDs on microscale display panels offer opportunities for the in-situ integration of micro-nano structure for light collimation. This means that device performance will be free of the limitations of the image source but directly correlated with the integrated display panel, while freeing up sufficient physical space to achieve a compact and flexible form factor. Therefore, the A-RPD exhibits great potential in exceeding traditional P-RPD and serves as an essential solution for AR devices. To date, several studies have demonstrated prototypes of the A-RPD as defined herein. However, the impact of the collimation characteristics on the practical performance of the integrated display panel-driven prototype has never been thoroughly discussed, which is fundamental to the principle of the A-RPD.

2.2 Theoretical derivation of the collimation-influenced DOF

DOF, conjugate to the depth of field, is a parameter used to evaluate the depth-dependent clarity of retinal imaging. Compared with other AR architectures, the expanded DOF stands as the most critical performance metric in RPD system design. A-RPD, as an architecture based on the same principle, also requires the minimized width of the projected beam onto the pupil, which is primarily governed by the collimation of pixelated light emission.

An ideal A-RPD theoretical model is illustrated in Fig. 2(a), comprising an integrated microscale display panel, a projection system, a 4-f system, and an eye model treated as an imaging system. In practical RPD devices, a beam splitter is typically employed to enable the overlapping of the projected image and real-world scenes, which is omitted here for clarity in fundamental optical path analysis. In this ideal configuration, the integrated microdisplay emits perfectly collimated light beams that sequentially pass through the pupil center and form an image on the retina modulated by the projection system and 4-f system. The practical model shows a similar optical path, but will create a broadening of the projected beams at the pupil from the light intensity distribution of the integrated microscale

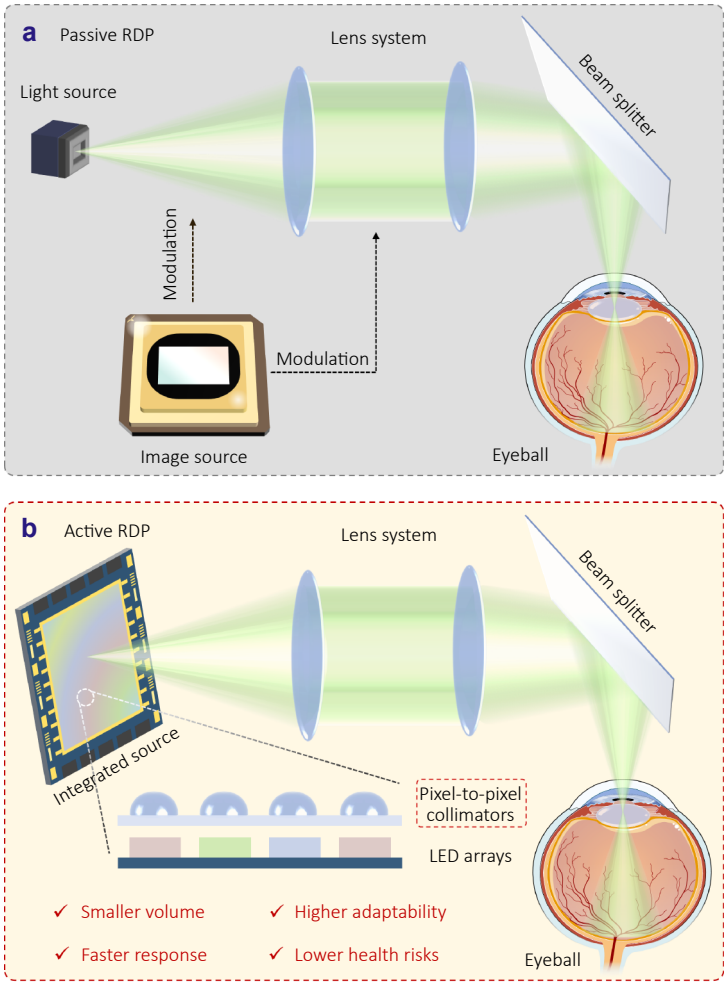

Fig. 1 | Definition of passive and active retinal projection display. The fundamental architecture of P-RPD (a) and A-RPD (b).

display panel and optical path in the system (Supplementary Section 1 and Eq. (1)). Therefore, the width of the beam at the pupil (d) can be primarily defined as

$$d \propto B \cdot \Delta\theta \,, \tag{1}$$

where B represents the optical path in the RPD system, which is extracted from the light propagation matrix (Supplementary Section 1); $\Delta\theta$ represents the divergence angle of the integrated microscale display panel, which is determined by the collimation of each pixel. It is noted that d is mainly determined by $\Delta\theta$ and leads to the undesirable DOF in this model. Thus, d is treated as a key parameter representing the light from RPD in the later derivation of DOF.

For further understanding and derivation of collimation-influenced DOF, we construct a fundamental model of the human eye and different projection models in the human eye (Fig. 2(b–d)). Figure 2(b) demonstrates the key parameters affecting DOF, including the minimum acceptable blur of the retina (δ), d, and d-influenced parameters: distance between the pupil and the retina (E) and the distance between the pupil and the point of the extended incident ray on the optical axis (K). When imperfectly collimated beams are projected onto the human eye, light rays influenced by the pupil converge either in front of or behind the retina. This results in different parameter values for defining the boundary conditions of the DOF (the focal length is denoted as f in derived equation), with the two corresponding models shown in Fig. 2(c) and Fig. 2(d). The cross-section of light rays transmitted by the RPD system in front of the pupil is selected as the object for the human eye system, with a certain object distance (l) and object height (y). Based on the geometric relationships and object-image relationships, the following can be derived:

$$y = \left(1 - \frac{l}{K}\right) \cdot d \,, \tag{2}$$

$$l' = \frac{f \cdot l}{f + l} \,, \tag{3}$$

$$y' = \frac{f \cdot y}{f + l} \,, \tag{4}$$

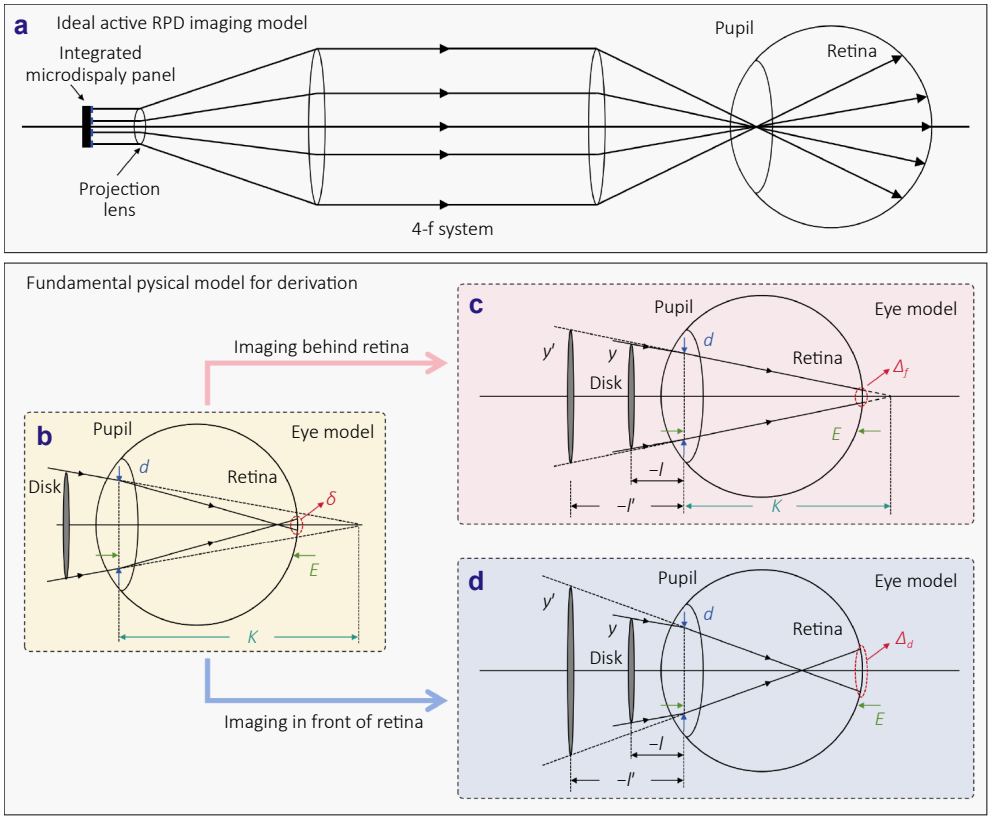

Fig. 2 | The model for theoretical derivation. (a) An ideal A-RPD imaging model based on the principle of the Maxwellian view display. (b) The key parameters influencing DOF in the eye model. (c, d) The derivation model of DOF with light rays converged either behind (c) or in front of the retina (d).

where l' represents image distance and y' is the image height. The blur degree of these two models (Δ_f for Fig. 2(c) and Δ_d for Fig. 2(d)) can be further derived based on geometric optics principles:

$$\Delta_f = \frac{E \cdot (y' - d)}{l'} + d\,, \tag{5}$$

$$\Delta_d = \frac{E \cdot (d - y')}{l'} - d\,. \tag{6}$$

This blur degree must fall within the range of the minimum acceptable blur of the retina (i.e., Δ_f and Δ_d both $< \delta$), thereby enabling the derivation of the lower and upper limits at a determined d:

$$\begin{aligned} &\frac{E}{1-\frac{E}{K}} - \frac{E}{1-\frac{E}{K}} \cdot \frac{\delta}{\left(1-\frac{E}{K}\right)\cdot d + \delta} < f \\ &< \frac{E}{1-\frac{E}{K}} + \frac{E}{1-\frac{E}{K}} \cdot \frac{\delta}{\left(1-\frac{E}{K}\right)\cdot d - \delta}\,. \end{aligned} \tag{7}$$

Further collation was performed to obtain the determination formula for the DOF, where retinal imaging remains clear:

$$DOF = \frac{2E\delta}{\left(1-\frac{E}{K}\right)^2 \cdot d - \frac{\delta^2}{d}}\,. \tag{8}$$

In this equation, K is a parameter related to d as mentioned above; specifically, the larger d is, the less the ratio of K to E approaches 1. This indicates that the DOF can be completely determined by d, which is influenced by the collimation of the A-RPD system. According to Eq. (8), while E and δ are still parameters that affect the DOF, they are fixed for an identical observer. Thus, this equation may serve as one of the most crucial guides for high-performance A-RPDs.

2.3 The verification of the collimation-influenced DOF

To validate the accuracy of the derived DOF equations, an eye model was constructed behind the A-RPD for optical simulation (Supplementary Table S1). The beam width d at the pupil was simulated by adjusting the aperture radius, indicating the influence of the integrated microdisplay panels with different collimation performance. The criterion for maintaining clear retinal imaging was set such that the root-mean-square (RMS) radius of the spot diagram is less than 2 μm (Supplementary Fig. S1 and Supplementary Table S2), considering the physical size of two adjacent cone

cells (4–6 μm). By continuously varying the beam width d, the corresponding variation values of the DOF upper and lower limits can be directly obtained from the simulation results. Considering the typical human pupil diameter ranges from 2 to 3 mm (Supplementary Table S3), the set variation range of d (0.2–1.2 mm) is sufficient to reflect the DOF changes regulated by d.

It is observed that as d gradually increases, the lower limit values of DOF rise while the upper limit values decline (Fig. 3(a) and 3(b)). This indicates that the DOF for clear retinal imaging shrinks as d increases, which aligns well with the preceding analysis (Fig. 3(c)). The theoretical fitting exhibits a high degree of alignment with the simulated values, following the derived inverse proportional function profile with $R^2 > 0.999$. The above comparative results demonstrate the accuracy of the derivation and analysis, and emphasize the importance of the collimation-affected d for the final retinal imaging from a data perspective.

2.4 The design of the microlens-based microscale display panels

In traditional methods, bulky lenses are typically used to collimate light sources, which is effective for point light sources with negligible size but unfavorable for display panel collimation. In miniaturized systems, the display panel size comparable to the collimator cannot be ignored, leading to attenuation of collimation performance at the edges. However, a single-pixel collimation scheme enables superior and uniform collimation performance through precise phase modulation at the pixel level, facilitating the realization of A-RPD architectures while enabling a broader DOF. Here, microlenses are chosen as candidates for integrated pixel-to-pixel collimation due to their simple fabrication process and excellent compatibility with microdisplay technologies.

A typical microlens-based micro-OLED model is shown in Fig. 4(a). Monochromatic micro-OLED display panels exhibit inconsistent pixel structures compared with full-color ones. The monochromatic micro-OLED display panels employ a single-color emission layer, while the full-color micro-OLED display panels are achieved through a white-light emission and trichromatic color filters. For design convenience, the independently driven sub-pixels are collectively treated as individual micro-OLEDs according to Fig. 4(a), thus simplifying the model. The individual micro-OLED model was configured with a Lambertian distribution and assumed in an ideal environment. All settings adhered to optical design requirements and will not affect the modulation of the light distribution emitted from the micro-OLED by the microlenses (Supplementary Table S4).

Here, we first define the angular range (θ_{50}) corresponding to the light intensity dropping to 50% as an index for quantitatively evaluating collimation performance. For an area light source that can be described by the Lambertian distribution formula, θ_{50} = 120°. Microlenses achieve collimation by converging light, resulting in increased brightness and reduced beam divergence. Considering the direction of light propagation, the microlenses are designed to have the same width as the top surface of the pixels. The optical collimation is regulated by adjusting the conic coefficient to modify the longitudinal profile of the microlenses. After optimization, the maximum height of the final microlens surface is determined at 2 μm. The simulated light distribution shows that, compared with micro-OLEDs without microlenses, those integrated with microlenses exhibit a significantly narrowed light distribution (Fig. 4(b) and Supplementary Fig. S2). The θ_{50} is significantly decreased to 50°.

Encouraged by the simulation results, we then obtained the micro-OLED display panels integrated with microlens arrays (MLAs). Microscopic images reveal that the microlens arrays exhibit a regular arrangement, while the white light interferometers characterize the MLAs with a maximum height of 2 μm and a period of 4 μm (Fig. 4(c, d)). Subsequently, we performed practical measurements on the light distribution of the micro-OLED display panels to verify the collimation effect of the MLAs.

Here, we selected two representative cross-sections (cross-sections a and b) of one sample to evaluate the overall light distribution of the micro-OLED display panels. Cross-sections a and b are perpendicular to each other, as

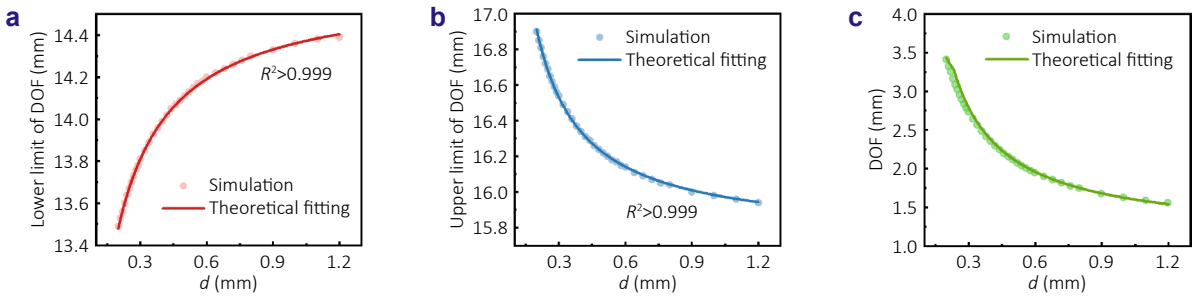

Fig. 3 | The simulation and fitting results for derived DOF. (a, b) The simulation and theoretically fitting results of lower (a) and upper (b) limits for derived DOF. (c) The simulation and theoretically fitting results of DOF.

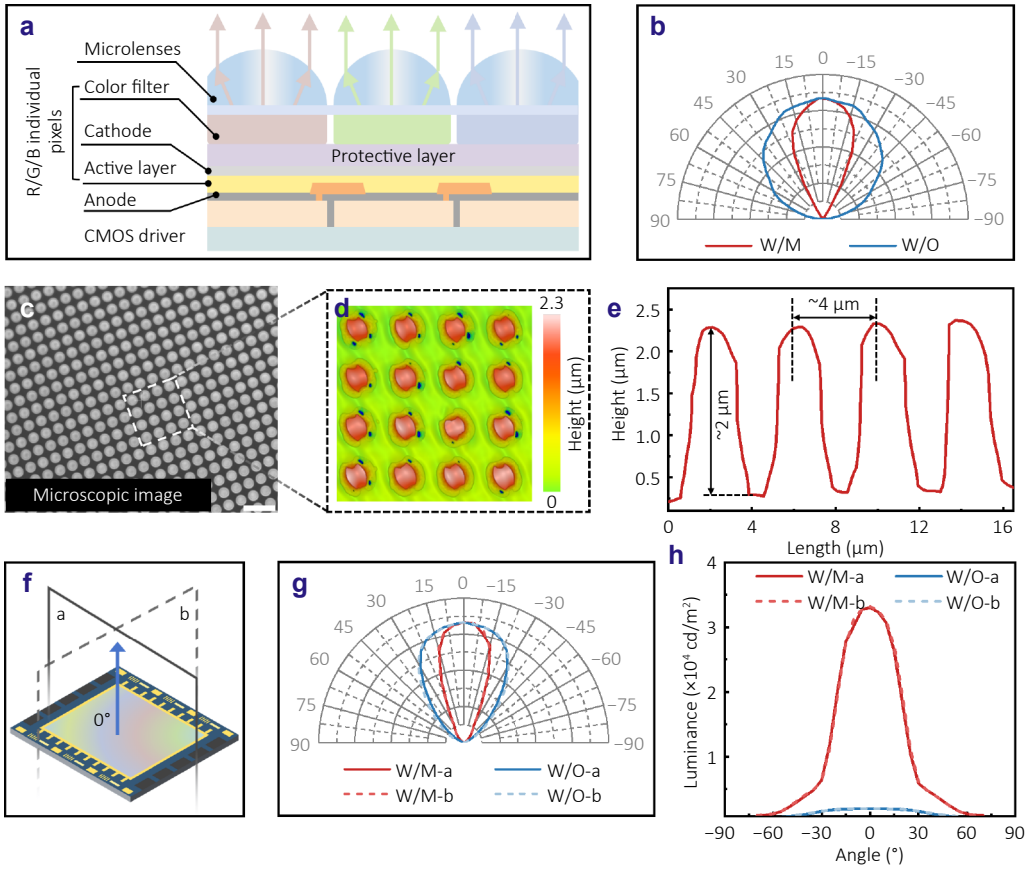

Fig. 4 | The simulation and practical results of micro-OLED with microlenese. (a) The schematic diagram of microlenses fabricated on micro-OLEDs with pixel-to-pixel alignment. (b) The simulation results of the collimation enabled by microlenses on micro-OLEDs. (c) The microscopic image of the obtained MLAs. (d, e) 2D profile (d) and height measurement curve (e) of microlens arrays. (f) The schematic diagram of representative cross-sections a and b. (g) The practical measurement of the light distribution of micro-OLED panels with or without MLAs. (h) The angle-dependent luminance of the micro-OLED panels with or without MLAs.

illustrated in Fig. 4(f). As clearly shown in Fig. 4(g), the micro-OLED display panels with MLAs (noted as W/M sample) exhibit a significantly narrower light distribution than the micro-OLED display panels without MLAs (noted as W/O sample) due to the light convergence by microlenses. The average θ_{50} is significantly decreased from 90° to 43°. Meanwhile, the profiles of cross-section a and cross-section b are highly consistent, demonstrating the excellent height uniformity of the MLA distribution (Fig. 4(g) and Supplementary Table S5). Furthermore, a more concentrated light intensity is achieved, which will be beneficial to enhancing the practical imaging performance under ambient light conditions (Fig. 4(h)).

2.5 The microlens-based A-RPDs

Benefiting from the collimated micro-OLED display panel at the pixel level, the A-RPD architecture can be successfully constructed (Fig. 5(a)). We first performed systematic simulation design for the A-RPD system, including a projection system, a 4-f system, and an eye model mentioned above (Supplementary Fig. S3(a)). After optimization, the obtained RPD system exhibits favorable imaging performance under the specified configuration. The final structure for practical construction is shown in the inset of Fig. 5(a), which is similar to the ideal structure described earlier but supplemented with the beam splitter.

The simulation results show that MTF of the designed A-RPD architecture exceeds 0.70 across all fields of view (FOV) at the spatial frequency of 30 lp mm^{-1} (Supplementary Fig. S3(b)). It should be emphasized that the MTF here is subject to multiple influences from the human eye model within the simulation model, resulting in final results significantly lower than those obtained without the eye model. Nevertheless, the results are sufficiently adequate to meet the requirements of retinal imaging (Supplementary Fig. S4 and Supplementary Table S6).

Based on the simulated results, we practically constructed the A-RPD prototype on the optical bench as shown in Fig. 5(a). The functional systems were placed according to the simulation model. A camera was positioned behind a beam-splitter to simulate the human eye, demonstrating the

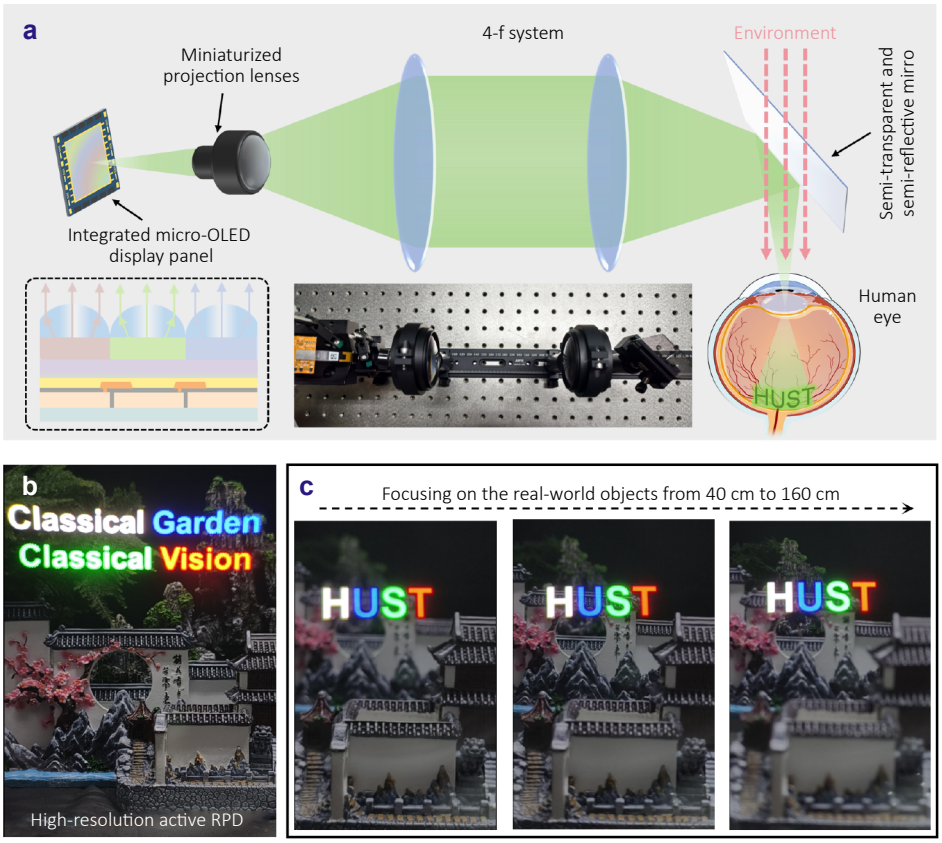

Fig. 5 | The practical construction of the microlenses-based A-RPD prototype. (a) The schematic diagram of the microlenses-based A-RPD prototype. The insets therein respectively show the schematic diagram of micro-OLEDs with in-situ integrated microlenses and the practical RPD prototype on an optical bench. (b) The high-resolution image projected by the A-RPD prototype. (c) The full-color retinal imaging from 40 cm to 160 cm.

imaging performance of the A-RPD prototype. Enlightened by the Chinese classical vision, we set some objects related to the classical garden in Suzhou. The specific location of each is shown in Supplementary Fig. S5.

For practical application, we proceeded to demonstrate the prototype with the MLA-integrated full-color micro-OLED display panel (Fig. 5(b)). The slight edge distortion in Fig. 5(b) can be further suppressed through algorithm optimization in practical applications. The A-RPD prototype maintains the high imaging performance with bright emission and clear boundary from 40 cm to 160 cm (Fig. 5(c) and Supplementary video). Meanwhile, this structure allows the preservation of high resolution with the original PPI and PPD of microscale display panels. The suitable design of the entire system enables the broadband white emission with negligible chromatic dispersion. As its excellent advantages, we emphasize that the A-RPD will be a promising solution in next-generation AR displays.

Additionally, we also offer the monochromatic demonstration to validate the retinal imaging based on the W/O or W/M samples. In Supplementary Fig. S6, the images projected by the W/O sample gradually become blurred with the focused objects varying from 40 cm to 160 cm. In contrast, the W/M sample enables the clear image projection under the same variation range (Supplementary Fig. S7). Additionally, the improved brightness can be easily observed in the A-RPD prototype, which may be attributed to the MLA-enhanced central intensity in Fig. 4(g).

3 Discussion

The A-RPD prototype, weighing < 280 g and measuring < 30 cm in length, provides an alternative for future AR devices (Supplementary Table S7). The optical elements in prototype can be further downscaled to back up the ultra-miniaturized devices. We emphasize that the A-RPD architecture holds great potential in display-on-chip systems and will facilitate the development of emerging display morphology's evolution, such as contact lens displays and transparent near-eye displays. Therefore, a thorough discussion of their future development is required.

Firstly, the collimated microscale display panel in A-RPDs serves to provide patterned and collimated light emission. In this work, by deriving the collimation-influenced DOF, we emphasize the necessity of integrated pixel-to-pixel collimators for future miniaturized devices. Although the separated

collimator arrays also hold the potential to realize A-RPDs like the fiber bundles, it should be noted that in-situ integrated collimators feature fewer light diffusion paths and a more compact volume, which will be advantageous in ultra-miniaturized AR devices[28,40].

The projection systems' further optimization and miniaturization have been carried out in mature waveguide-based AR systems. Its combination with the subsequent 4-f system serves to relay the expanded image to pass through the pupil center in this system. Herein, the 4-f system, as an important component, realizes off-axis beam extension and pupil relaying. Such multifunctional optical components are well-suited to be replaced by diffractive optical elements, which can significantly reduce the required volume of the system[31,41,42]. With the reduction of optical paths and achievements in microscale and nanoscale display panels, non-off-axis structures will further reduce the dependence on these two systems.

The inherent limitations of the Maxwellian-view principle make A-RPDs still face the challenge of a restricted eyebox. Two mainstream approaches previously developed for P-RPD architectures can be directly adapted to address this issue: eye-tracking and viewpoint replication. Eye-tracking relies on detecting the pupil center to ensure that light passes through it, whereas viewpoint replication employs optical elements to realize an expanded eyebox. Eye-tracking will enable A-RPD systems to adapt the commercialization requirements, while the rapid advances of diffractive optical elements endow viewpoint replication with substantial potential for ultra-compact devices[18,19,23].

4 Conclusion

In summary, we first propose the concept of the A-RPD. Through theoretical derivation and optical simulation, we clarify the collimation-influenced DOF of the A-RPD. As the collimation of pixelated microscale display panels improves, the DOF will gradually increase, thereby enabling clear retinal imaging within a certain zoom range. Leveraging increasingly mature pixel-to-pixel microlens collimators, we achieve a collimated micro-OLED display panel at the pixel level. Based on this display panel, a prototype of the A-RPD is successfully constructed. This prototype can realize clear retinal imaging from 40 cm to 160 cm. As near-eye displays evolve toward being compact, lightweight, and highly efficient, the proposal and standardization of the A-RPD are highly expected to become an important architecture for next-generation AR displays.

References

1. Xiong JH, Hsiang EL, He ZQ et al. Augmented reality and virtual reality displays: emerging technologies and future perspectives. *Light Sci Appl* **10**, 216 (2021).
2. Liu ZY, Wang DY, Gao H et al. Metasurface-enabled augmented reality display: a review. *Adv Photonics* **5**, 034001 (2023).
3. Cheng DW, Wang QW, Liu Y et al. Design and manufacture AR head-mounted displays: a review and outlook. *Light Adv Manuf* **2**, 350–369 (2021).
4. Gopakumar M, Lee GY, Choi S et al. Full-colour 3D holographic augmented-reality displays with metasurface waveguides. *Nature* **629**, 791–797 (2024).
5. Fan ZB, Cheng YF, Chen ZM et al. Integral imaging near-eye 3D display using a nanoimprint metalens array. *eLight* **4**, 3 (2024).
6. Tian ZT, Zhu XL, Surman PA et al. An achromatic metasurface waveguide for augmented reality displays. *Light Sci Appl* **14**, 94 (2025).
7. Choi S, Jang C, Lanman D et al. Synthetic aperture waveguide holography for compact mixed-reality displays with large étendue. *Nat Photonics* **19**, 854–863 (2025).
8. Moon S, Kim S, Kim J et al. Single-layer waveguide displays using achromatic metagratings for full-colour augmented reality. *Nat Nanotechnol* **20**, 747–754 (2025).
9. Sim I, Choi K, Baek Y et al. Microdisplay technologies in augmented reality and virtual reality headsets. *Nat Rev Electr Eng* **2**, 634–650 (2025).
10. Chen BQ, Li C, Li XX et al. SiC diffractive waveguides for augmented reality: single-layer, full-color, rainbow-artifact-free display with vision correction. *eLight* **5**, 21 (2025).
11. Hu GY, Pei CY, Sun HT et al. Design and fabrication of a compact augmented reality near-eye display with freeform holographic optics. *Opt Express* **33**, 22431–22441 (2025).
12. Chang W, Kim J, Kim M et al. Concurrent self-assembly of RGB microLEDs for next-generation displays. *Nature* **617**, 287–291 (2023).
13. Hsiang EL, Yang ZY, Yang Q et al. AR/VR light engines: perspectives and challenges. *Adv Opt Photonics* **14**, 783–861 (2022).
14. Spiegel DP, Erkelens IM. Vergence-accommodation conflict increases time to focus in augmented reality. *J Soc Inf Disp* **32**, 194–205 (2024).
15. Yin K, He ZQ, Xiong JH et al. Virtual reality and augmented reality displays: advances and future perspectives. *J Phys Photonics* **3**, 022010 (2021).
16. Do H, Kim YM, Min SW. Focus-free head-mounted display based on Maxwellian view using retroreflector film. *Appl Opt* **58**, 2882–2889 (2019).
17. Wang YD, Yang T, Lyu X et al. Large depth-of-field, large eyebox, and wide field-of-view freeform-holographic augmented reality near-eye display. *Adv Sci* **12**, e08773 (2025).
18. Zou JY, Li LS, Wu ST. Gaze-matched pupil steering maxwellian-view augmented reality display with large angle diffractive liquid crystal lenses. *Adv Photonics Res* **3**, 2100362 (2022).
19. Lin TG, Zhan T, Zou JY et al. Maxwellian near-eye display with an expanded eyebox. *Opt Express* **28**, 38616–38625 (2020).
20. Chen CP, Zhou L, Ge JH et al. Design of retinal projection displays enabling vision correction. *Opt Express* **25**, 28223–28235 (2017).
21. Takaki Y, Fujimoto N. Flexible retinal image formation by holographic Maxwellian-view display. *Opt Express* **26**, 22985–22999 (2018).
22. Shrestha PK, Pryn MJ, Jia J et al. Accommodation-free head mounted display with comfortable 3D perception and an enlarged eye-box. *Research* **2019**, 9273723 (2019).
23. Jiang HN, Cheng YC, Sun ZB et al. Pupil-adaptive retina projection augment reality displays with switchable ultra-dense viewpoints. *Adv Sci* **12**, 2416961 (2025).
24. Qian YZ, Yang ZY, Huang YH et al. Directional high-efficiency nanowire LEDs with reduced angular color shift for AR and VR displays. *Opto-Electron Sci* **1**, 220021 (2022).
25. Lian YX, Wang YX, Yuan YC et al. Downscaling micro- and nano-

perovskite LEDs. *Nature* **640**, 62–68 (2025).
26. Li ZC, Liu YB, Jiang HN et al. Vertical GaN-On-GaN micro-LEDs for near-eye displays. *Adv Sci* **12**, e06784 (2025).
27. Meng WQ, Xu FF, Yu ZH et al. Three-dimensional monolithic micro-LED display driven by atomically thin transistor matrix. *Nat Nanotechnol* **16**, 1231–1236 (2021).
28. Chen EG, Fan ZG, Zhang KX et al. Broadband beam collimation metasurface for full-color micro-LED displays. *Opt Express* **32**, 10252–10264 (2024).
29. Aratani S, Adachi M, Shimizu M et al. Collimated light source using patterned organic light-emitting diodes and microlens. *Jpn J Appl Phys* **49**, 042101 (2010).
30. Freitas JR, Pimenta S, Ribeiro JF et al. Simulation, fabrication and morphological characterization of a PDMS microlens for light collimation on optrodes. *Optik* **227**, 166098 (2021).
31. Yin K, Hsiang EL, Zou JY et al. Advanced liquid crystal devices for augmented reality and virtual reality displays: principles and applications. *Light Sci Appl* **11**, 161 (2022).
32. Chen HW, Lee JH, Lin BY et al. Liquid crystal display and organic light-emitting diode display: present status and future perspectives. *Light Sci Appl* **7**, 17168–17168 (2018).
33. Hsiang EL, Yang Q, He ZQ et al. Halo effect in high-dynamic-range mini-LED backlit LCDs. *Opt Express* **28**, 36822–36837 (2020).
34. Chen HW, Zhu RD, Li MC et al. Pixel-by-pixel local dimming for high-dynamic-range liquid crystal displays. *Opt Express* **25**, 1973–1984 (2017).
35. Huang YG, Hsiang EL, Deng MY et al. Mini-LED, micro-LED and OLED displays: present status and future perspectives. *Light Sci Appl* **9**, 105 (2020).
36. Miao WC, Hsiao FH, Sheng YJ et al. Microdisplays: mini-LED, micro-OLED, and micro-LED. *Adv Opt Mater* **12**, 2300112 (2024).
37. Liu YB, Wang GB, Feng F et al. Ultra-low-defect homoepitaxial micro-LEDs with enhanced efficiency and monochromaticity for high-PPI AR/MR displays. *PhotoniX* **5**, 23 (2024).
38. Zhan T, Xiong JH, Zou JY et al. Multifocal displays: review and prospect. *PhotoniX* **1**, 10 (2020).
39. Luo ZY, Ding YQ, Peng FL et al. Ultracompact and high-efficiency liquid-crystal-on-silicon light engines for augmented reality glasses. *Opto-Electron Adv* **7**, 240039 (2024).
40. Chen EG, Zhao MY, Chen KK et al. Metamaterials for light extraction and shaping of micro-scale light-emitting diodes: from the perspective of one-dimensional and two-dimensional photonic crystals. *Opt Express* **31**, 18210–18226 (2023).
41. Li Y, Chen SY, Liang HW et al. Ultracompact multifunctional metalens visor for augmented reality displays. *PhotoniX* **3**, 29 (2022).
42. Chen QK, Zhou JC, Pian S et al. Hybrid meta-optics enabled compact augmented reality display with computational image reinforcement. *ACS Photonics* **11**, 3794–3803 (2024).

Acknowledgements

The authors acknowledge support from the National Natural Science Foundation of China (62322505, 62374069), the National Key Research and Development Program of China (2024YFA1209503), the Open Project Program of Wuhan National Laboratory for Optoelectronics (2023WNLOKF011), and the key R&D program from Hubei Province (2024BAA004). We thank Mr. B. Liu, Mr. X. Li, and other engineers from SeeYA Technology Co., Ltd. for providing access to conduct the fabrication of the integrated MLAs. We thank valuable suggestions from H. Jin, H. Chen, W. Lai, and X. Su at Fuzhou University. We also thank helpful discussions from Q. He at Southeast University and Dr. N. Liu at Wuhan Textile University.

Author contributions

X.Z., Y.H., and J.L. conceived the study. J.L. supervised the study. X.Z. and Y.H. performed the theoretical derivation and optical simulation. X.Z., Y.H., and W.F. conducted the practical construction of the A-RPD prototype. X.Z., Y.H., E.C., and J.L. wrote the paper. All of the authors contributed to the final version of this paper.

Competing interests

The authors declare no competing financial interests.

Data availability

The data that support the plots within this paper and other findings of this study are available from the corresponding author upon reasonable request.

Supplementary information

Supplementary information for this paper is available at
https://doi.org/10.29026/oea.2026.250252